Thermal Evolution of Dirac Magnons in the Honeycomb Ferromagnet $CrBr_3$

S. E. Nikitin,[1,*] B. Fåk,[2] K. W. Krämer,[3] T. Fennell,[4] B. Normand,[5,6] A. M. Läuchli,[5,6] and Ch. Rüegg[1,6,7,8]
[1]Quantum Criticality and Dynamics Group, Paul Scherrer Institute, CH-5232 Villigen-PSI, Switzerland
[2]Institut Laue-Langevin, 71 avenue des Martyrs, CS 20156, F-38042 Grenoble Cedex 9, France
[3]Department of Chemistry, Biochemistry and Pharmacy, University of Bern, Freiestrasse 3, CH-3012 Bern, Switzerland
[4]Laboratory for Neutron Scattering and Imaging, Paul Scherrer Institute, CH-5232 Villigen, Switzerland
[5]Laboratory for Theoretical and Computational Physics, Paul Scherrer Institute, CH-5232 Villigen-PSI, Switzerland
[6]Institute of Physics, Ecole Polytechnique Fédérale de Lausanne (EPFL), CH-1015 Lausanne, Switzerland
[7]Institute for Quantum Electronics, ETH Zürich, CH-8093 Hönggerberg, Switzerland
[8]Department of Quantum Matter Physics, University of Geneva, CH-1211 Geneva, Switzerland

(Received 24 April 2022; accepted 17 August 2022; published 13 September 2022)

$CrBr_3$ is an excellent realization of the two-dimensional honeycomb ferromagnet, which offers a bosonic equivalent of graphene with Dirac magnons and topological character. We perform inelastic neutron scattering measurements using state-of-the-art instrumentation to update 50-year-old data, thereby enabling a definitive comparison both with recent experimental claims of a significant gap at the Dirac point and with theoretical predictions for thermal magnon renormalization. We demonstrate that $CrBr_3$ has next-neighbor J_2 and J_3 interactions approximately 5% of J_1, an ideal Dirac magnon dispersion at the K point, and the associated signature of isospin winding. The magnon lifetime and the thermal band renormalization show the universal T^2 evolution expected from an interacting spin-wave treatment, but the measured dispersion lacks the predicted van Hove features, pointing to the need for more sophisticated theoretical analysis.

DOI: 10.1103/PhysRevLett.129.127201

Graphene, the original two-dimensional (2D) material, is a single layer of carbon atoms with strong covalent bonds forming a honeycomb lattice, and some of its exceptional physical properties [1–3] are a consequence of its band-structure topology, which allows the electrons to behave as massless quasiparticles described by the Dirac equation. The same band structure is realized for bosonic quasiparticles in systems such as a 2D ferromagnet (FM) on the honeycomb lattice [4] shown in Fig. 1(a), which has magnon excitations that also exhibit Dirac cones at the K points of the Brillouin zone (BZ), as represented in Figs. 1(b) and 1(c). The topology of magnon band structures has became a matter of active theoretical [4–8] and experimental [9–14] research due to possible applications in spintronic devices [15–17]. Inelastic neutron scattering (INS) provides direct access to the magnon dispersion, and the spectra of a number of honeycomb FMs have been measured in their low-temperature regimes ($T \ll T_c$, the temperature of magnetic order) [10,12,18].

Promising materials for these studies are the family of chromium trihalides, CrX_3 (X = Cl [23], Br [24], I [25]), in which the honeycomb layers [Fig. 1(a)] have identical stacking, but T_c, the size, and even the sign of the interlayer magnetic interaction all vary with X [26]. Measurements on $CrCl_3$ [18,27] indicate a Dirac-cone magnon dispersion [Fig. 1(b)], but in CrI_3 a gap is reported [10] at the K point, creating acoustic and optical magnon modes [Fig. 1(c)] whose anticrossing is thought to be a consequence of strong next-neighbor Dzyaloshinskii-Moriya (DM) interactions. $CrBr_3$ was for 50 years considered as a textbook example of FM magnons, with no indication for a band splitting [24,28], but the recent report of a large, DM-induced anticrossing [13] similar to CrI_3 has created controversy. Turning to the temperature-induced renormalization of these magnons, theoretical calculations predicted that a Dirac-cone spectrum should produce a very specific T^2 form for the evolution of the magnon dispersion and linewidth [4], accompanied by characteristic features at certain wave vectors. Although the old INS results were cited as verification, systematic measurements of the thermal renormalization of the magnon spectrum remain absent.

In this Letter, we perform a comprehensive study of the temperature-induced renormalization of the magnon self-energy in $CrBr_3$ using modern neutron spectrometers. We first use low-temperature INS data to refine the magnetic spin Hamiltonian and find weak next-neighbor interactions. We prove that the magnon dispersion has Dirac cones, the recent report to the contrary apparently being an artifact of the data treatment, and we demonstrate near-ideal cosinusoidal intensity winding around the K points. Working at temperatures up to 40 K, we find considerable downward renormalization of the magnon dispersion and growing linewidths, whose T^2 form we characterize to high accuracy, but whose variation across the BZ is demonstrably not well captured by the available theory. In this way our results

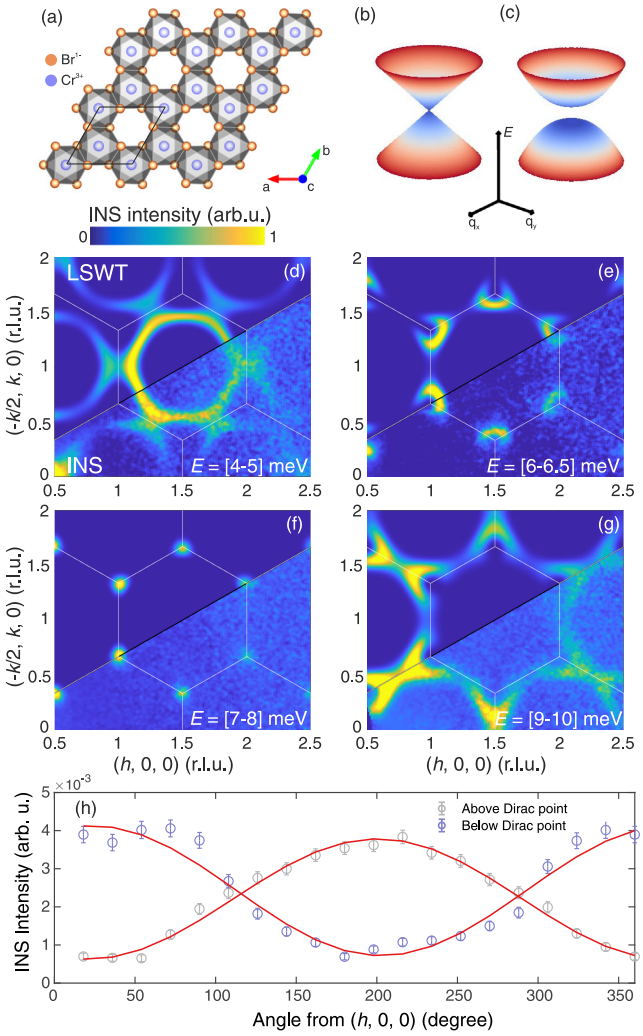

FIG. 1. (a) Honeycomb layer of $CrBr_3$. The Cr^{3+} ions (blue) host $S = 3/2$ spins with FM interactions. (b),(c) Schematic spin-wave spectra in the vicinity of the K points. When inversion symmetry is preserved, the dispersion forms a Dirac cone (b); otherwise, a gap opens to form separate acoustic and optical magnon branches (c). (d)–(g) Scattered intensity obtained by integrating the PANTHER $E_i = 30$ meV dataset over four constant-energy windows (indicated) and compared with linear spin-wave theory (LSWT); all panels have the same intensity scale. White lines indicate the boundaries of the crystallographic BZ. A **Q**-independent background was subtracted from each spectrum to aid visual comparison. (h) Intensity obtained on winding around the K point, showing a cosinusoidal modulation with inverted phase for energies above and below the Dirac point. Solid lines show the corresponding fits [Supplemental Material Eq. (S1) [19]] with an additive background term.

establish the experimental standard for temperature-induced modification of the spin dynamics in a honeycomb ferromagnet.

Experiment.—A 1.5 g single crystal of $CrBr_3$ was grown by slow sublimation in a temperature gradient under vacuum, as detailed in Sec. S1 of the Supplemental Material (SM) [19]. Its high quality was confirmed by single-crystal neutron diffraction, from which we determined the lattice parameters at 1.7 K as $a = b = 6.31$ Å and $c = 18.34$ Å, and a structure consistent with the BiI_3-type and space group $R\bar{3}$ [23,24]. We conducted two INS experiments, using the time-of-flight (TOF) spectrometer PANTHER at the Institut Laue-Langevin [29,30] and the triple-axis spectrometer (TAS) EIGER at the Paul Scherrer Institute [31]. In both experiments the sample was oriented in the $(hk0)$ scattering plane. On PANTHER we collected data at $T = 1.7$, 20, 30, and 40 K, each with two incident neutron energies, $E_i = 15$ and 30 meV, and performed TOF data reduction and analysis using the software MANTID [32] and HORACE [33]. On EIGER we used the fixed-k_f mode and worked at eight different temperatures from 1.5 to 40 K. Resolution information for both instruments is discussed in Sec. S2 of the SM [19]. Calculations of the low-temperature magnon dispersion and intensity, which we used to fit the spin Hamiltonian, were performed using the SPINW package [34].

Low-temperature spectra.—We begin with the spectra collected on PANTHER at $T = 1.7$ K, a temperature much smaller than $T_c = 32$ K [13,35] and thus fully representative of the ground-state properties. Figures 1(d)–1(g) show constant-energy cuts at four different parts of the magnon spectral function and Figs. 2(b)–2(d) show momentum-energy cuts for several high-symmetry paths in the BZ [Fig. 2(a)]. We also used the vertical detector coverage to confirm dispersionless behavior in the out-of-plane direction, as shown in Sec. S2A of the SM [19]. Focusing first on the two M-K-Γ paths in Figs. 2(b) and 2(c), both spectra exhibit a sharp, continuous, and resolution-limited magnon mode with a bandwidth of approximately 10 meV, a parabolic dispersion around Γ, and different intensities in the two zones shown. Figures 2(c) and 2(d) show the second magnon branch in the crystallographic BZ dispersing from 5 to 13 meV, although with zero intensity in Fig. 2(b), and we refer to the two branches as modes 1 and 2. Here, we label all high-symmetry points according to the crystallographic BZ, but stress that the modulation of the scattered intensity follows the unfolded zone shown in Fig. 2(a), leading to the intensity variations between BZs in Figs. 1 and 2.

Our first key result is the unambiguous demonstration of the data in Figs. 2(b) and 2(c) that the magnon bands have a Dirac dispersion through the K point, with no detectable splitting into acoustic and optical modes. It is important to contrast this conclusion with the recent INS study of Ref. [13], which reported a large band splitting at the K point. In Sec. S2B of the SM [19] we demonstrate that the reported splitting is not intrinsic to $CrBr_3$, but is rather an artifact arising from the large integration width applied in the analysis of the TOF dataset [27].

Thus, we conclude that the low-temperature magnon dispersion in $CrBr_3$ has an ideal Dirac-cone nature with the Dirac point at 7.5 ± 0.1 meV [Fig. 1(f)]. This is fully

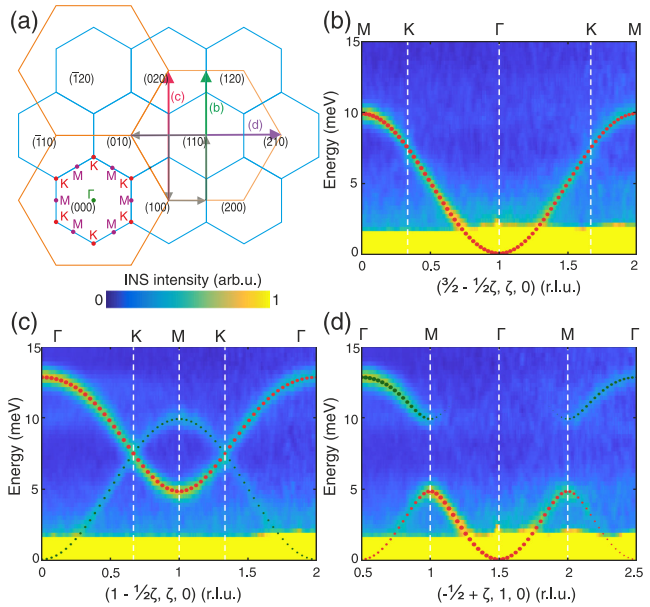

FIG. 2. Low-temperature magnon dispersion measured along several high-symmetry directions. (a) Reciprocal-space representation of the honeycomb lattice in the $(hk0)$ plane showing the crystallographic BZ in blue and the unfolded zone in orange. Green, red, and violet arrows indicate the paths for the spectra shown, respectively, in panels (b)–(d); the gray arrow indicates the complete path used in Fig. 3. (b)–(d) Spin-wave spectra collected using PANTHER with $E_i = 30$ meV at $T = 1.7$ K. The data were integrated by ± 0.03 r.l.u. along the orthogonal in-plane direction and ± 5 r.l.u. in the out-of-plane l direction. Red and green points show, respectively, the dispersions of modes 1 and 2 modeled by LSWT and their sizes represent the calculated intensities.

consistent with the inversion symmetry of the nearest-neighbor bond and the conventional g-factor values, both of which exclude significant DM effects. It is also consistent with all of the early INS results [24,28], as we show in Sec. S2C of the SM [19]. The Dirac cone in the 2D honeycomb FM was also used as a test case for the theoretical prediction [36] of a cosinusoidal intensity modulation arising from the isospin winding of near-nodal quasiparticles. This fingerprint has been observed recently in the honeycomb material $CoTiO_3$ [12] and in elemental Gd [14], and our results for the intensity distribution around the K point, shown in Fig. 1(h) and detailed in Sec. S2D of the SM [19], constitute its cleanest observation to date.

Next, we use our low-temperature INS spectra to refine the spin Hamiltonian. Based on the lack of evidence for DM interactions in Fig. 2, but the very accurate measurement of a tiny spin gap at the Γ point by ferromagnetic resonance (FMR) [35,37], we consider a Heisenberg model with single-ion anisotropy,

$$\mathcal{H} = \sum_{\langle i,j \rangle} J_{ij} \mathbf{S}_i \cdot \mathbf{S}_j + D \sum_i (S_i^z)^2. \tag{1}$$

Here, $\mathbf{S}_i$ is a $S = 3/2$ spin operator, J_{ij} are isotropic superexchange interactions between different Cr-ion pairs, and D is the single-ion term. We determine the energies of the two magnon modes at 139 $\mathbf{Q}$ points by fitting the corresponding constant-$\mathbf{Q}$ cuts to two resolution-convolved Lorentz functions. We then use this dataset to fit the magnetic interactions in $CrBr_3$ by working within LSWT, as implemented in SPINW. We find the most accurate description of the observed spectra using three in-plane interactions and a very weak easy-axis anisotropy, as detailed in Sec. S3 of the SM [19]. The optimal parameters we obtain for Eq. (1) are $J_1 = -1.485(15)$, $J_2 = -0.077(13)$, $J_3 = 0.068(12)$, and $D = -0.028(7)$ meV. Although we cannot detect the spin gap created by such a small anisotropy, we include the gap deduced from FMR in our fit. The excellent agreement between the observed and calculated INS spectra, both in dispersion and intensity distribution, is clear in Figs. 1(d)–1(g) and 2(b)–2(d).

Spin dynamics at finite temperature.—Turning to thermal effects, Figs. 3(a) and 3(b) show two representative spectra collected, respectively, at $T = 1.7$ and 30 K. Increasing T clearly broadens the magnons and causes a downward energy shift, which decreases their bandwidth. To quantify both effects, and their dependence on $\mathbf{Q}$, we used PANTHER to measure the spectral function at $T = 20$, 30, and 40 K over several BZs. We made multiple constant-$\mathbf{Q}$ cuts covering four high-symmetry directions and fitted each peak with a Lorentzian broadening, convolved with the experimental resolution, to extract the positions and widths of the two magnon modes at each T and $\mathbf{Q}$ point. Figure 3(c) summarizes the mode positions obtained at all four temperatures.

To visualize the effect of temperature on the magnon bands, we compute the normalized dispersion shift [28]

$$\Delta\tilde{\varepsilon}_{\mathbf{q}}(T) = \frac{\varepsilon_{\mathbf{q}}(0) - \varepsilon_{\mathbf{q}}(T)}{\varepsilon_{\mathbf{q}}(0) T^2}, \tag{2}$$

where $\varepsilon_{\mathbf{q}}(0)$ denotes the dispersion measured at base temperature and $\varepsilon_{\mathbf{q}}(T)$ the corresponding finite-T result. In the interacting SWT analysis of Ref. [4], the T-induced dispersion renormalization consists of a real Hartree term, $\Sigma_1(\mathbf{q})$, with a weak $\mathbf{q}$ dependence caused only by J_2, and a "sunset" term, $\Sigma_2(\mathbf{q})$. Because both are expected to show a T^2 form [4,38], we have included this factor in Eq. (2).

The symbols in Fig. 3(d) show the dispersion renormalization along the high-symmetry paths. The data for different temperatures collapse rather well to a single curve for both modes over the majority of the BZ, and we find that no change to the assumed T^2 form improves this collapse. To interpret this result, we have adapted the calculations of Ref. [4] to include the J_2 and J_3 terms, and present the details of this adaptation in Sec. S4 of the SM [19]. We observe that $\Delta\tilde{\varepsilon}_{\mathbf{q}}(T)$ for the upper branch is

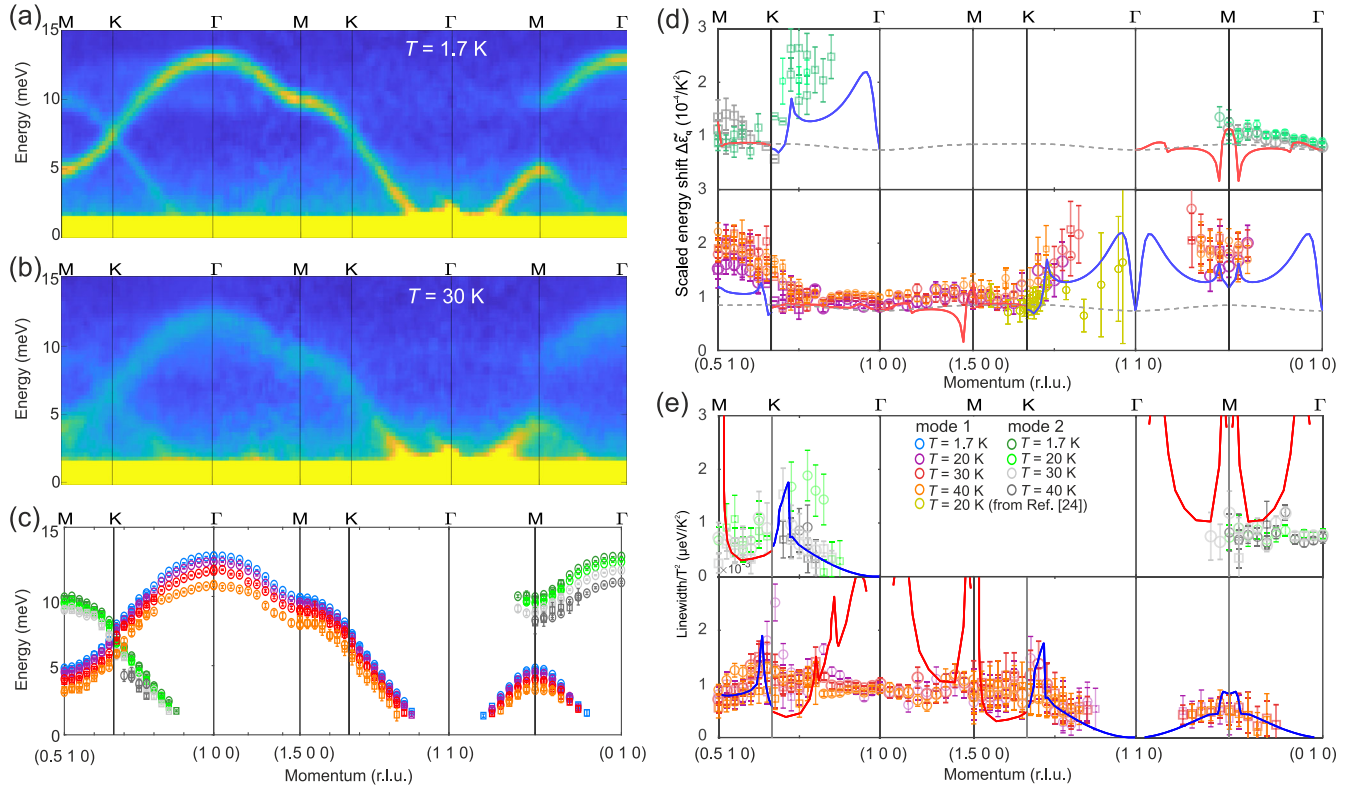

FIG. 3. Thermal magnon renormalization in $CrBr_3$. (a),(b) Magnon spectra for the high-symmetry directions taken from the PANTHER $E_i = 30$ meV dataset at $T = 1.7$ K (a) and $T = 30$ K (b). The data were integrated over ± 0.015 Å^{-1} in-plane and ± 2 Å^{-1} for l. (c) Magnon branches 1 and 2 extracted for the four experimental temperatures; circles were taken from the $E_i = 30$ meV dataset and squares from $E_i = 15$ meV. The mode intensities vanish in some regions of the unfolded BZ. (d) Temperature-induced renormalization of the measured magnon dispersions for modes 1 (up) and 2 (down), shown in the reduced form of Eq. (2). Solid lines show the real part of the self-energy, $\mathrm{Re}\Sigma(\mathbf{q})$, obtained by adapting the analytical framework of Ref. [4], in which calculations are performed for the upper (red) and lower (blue) bands in the crystallographic BZ; dashed lines show the Hartree term, $\Sigma_1(\mathbf{q})$. (e) Reduced thermal renormalization of the measured magnon linewidths for modes 1 (up) and 2 (down). Solid lines show $-\mathrm{Im}\Sigma(\mathbf{q})$ obtained following Ref. [4].

described largely by the Hartree term alone, with the $\Sigma_2(\mathbf{q})$ contribution becoming sizable only below the Dirac point.

Similarly, Fig. 3(e) demonstrates the analogous T^2 data reduction for the magnon linewidth. Again, the experimental results for all temperatures collapse rather well, within their own uncertainties, to a single line. In this case, J_2 and J_3 have a qualitative role in removing linewidth divergences that appear at the Γ and M points due to the perfect nesting of the nearest-neighbor bands [4]. However, even with these terms, the interacting SWT analysis predicts that both the linewidth and the band renormalization [Fig. 3(d)] should show multiple sharp peaks across the BZ, these "van Hove" features reflecting the underlying bare magnon bands [4], whereas our data do not support their presence.

A striking example is the difference between our data and the adapted SWT treatment around the M point, where the analysis predicts that both the energy and linewidth of the 10 meV peak should show a sharp cusp, which is shifted slightly from M due to J_2 and J_3 [red lines in Figs. 3(d) and 3(e)]. To analyze the thermal renormalization in a fully quantitative manner, we used EIGER to measure the spectrum at the M point $\mathbf{Q} = (1.5\,0\,0)$ for multiple temperatures up to 40 K, as shown in Fig. 4(a). Figures 4(b) and 4(c) show, respectively, the dependences on T of the magnon energy and linewidth extracted from both EIGER and PANTHER datasets. When fitted to the form $a + bT^{\alpha}$, the M-point data yield $\alpha_{\mathrm{energy}} = 2.25(15)$ and $\alpha_{\mathrm{width}} = 1.95(14)$, in good agreement with the expected value $\alpha = 2$. The same fitting at several $\mathbf{Q}$ points around $(1.5\,0\,0)$ also yields quadratic forms for both quantities [Figs. 4(b) and 4(c)], while the prefactors b that we extract show no appreciable changes with $\mathbf{Q}$ in Fig. 4(d), quite in contrast to interacting SWT.

Discussion.—Our studies of thermal renormalization verify an ideal T^2 form, in fact above as well as below T_c, as we have demonstrated in particular detail at the M point (Fig. 4). The origin of this behavior lies in the 2D nature of $CrBr_3$ and the quadratic dispersion at the band minimum, where thermally activated magnons cause the interaction effects responsible for band renormalization [38]. By a T^2 data reduction across the whole BZ, we find that the finite-T magnon bands we have measured at high $\mathbf{q}$

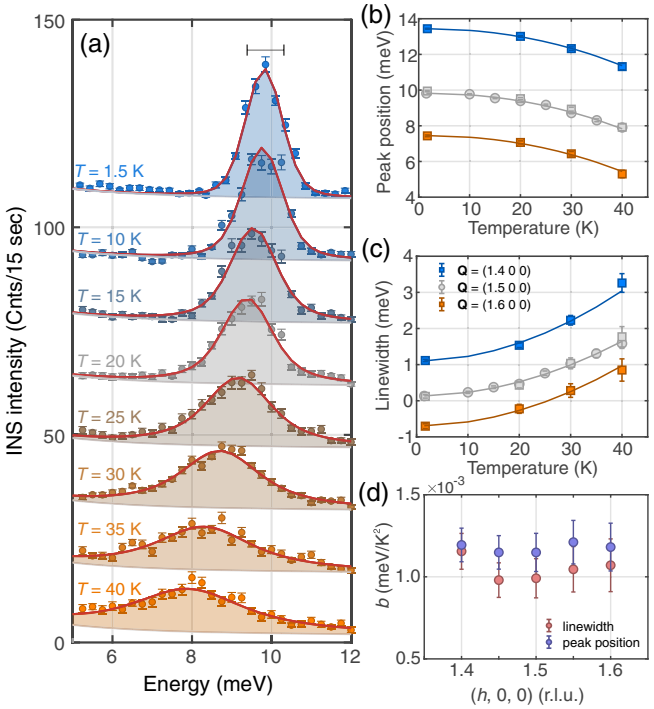

FIG. 4. Thermal magnon renormalization at the M point. (a) Constant-$\mathbf{Q}$ cuts measured on EIGER at the M point, $\mathbf{Q} = (1.5\,0\,0)$. Spectra for the different temperatures are offset vertically by +15 units for clarity. Red lines show complete fits to the data composed of a magnon contribution (shaded areas) and a temperature-independent background. The horizontal bar indicates the FWHM resolution of EIGER at 10 meV. (b),(c) Dependence of the peak position (b) and linewidth (c) on temperature; solid lines show quadratic fits. Squares and circles correspond, respectively, to results obtained by fitting the PANTHER and EIGER datasets. (d) $\mathbf{Q}$ dependence of the quadratic fitting coefficients b through the M point.

resolution do not show features at the characteristic wave vectors found in a SWT analysis. This indicates that the $S = 3/2$ honeycomb FM is subject to complex renormalization effects, arising from the combination of quantum and thermal fluctuations in the restricted phase space, whose accurate calculation calls for a more advanced (self-consistent and perhaps constrained) spin-wave treatment or for an unbiased numerical analysis by state-of-the-art quantum Monte Carlo [39,40] or matrix-product techniques [41,42].

To conclude, we have applied modern neutron spectrometry and data analysis to the layered honeycomb $S = 3/2$ ferromagnet $CrBr_3$. At the band minimum we demonstrate quadratically dispersing magnons with a spin gap far below our base temperature. At the K point we demonstrate a near-perfect Dirac-cone dispersion with no discernible gapping, and we show that its topological consequences are reflected in the intensity winding. We obtain an accurate fit of the weak next-neighbor Heisenberg interactions, which remove the perfect honeycomb band nesting. At finite temperatures, the magnon renormalization obeys the expected T^2 form to very high accuracy. However, its dependence on the wave vector is not well reproduced at low order in spin-wave theory, indicating a need for more systematic calculations of mutual quantum and thermal renormalization effects in low-dimensional magnetism.

We acknowledge financial support from the Swiss National Science Foundation. C. R. is grateful to the European Research Council for the support of grant Hyper Quantum Criticality (HyperQC) and SEN to the European Union Horizon 2020 research and innovation program for Marie Sklodowska-Curie Grant No. 884104. This work is based on experiments performed at the Institut Laue-Langevin (ILL), Grenoble, France, and at the Swiss spallation neutron source SINQ, Paul Scherrer Institute (PSI), Villigen, Switzerland.

Note added.—We recently became aware that the data-analysis problem affecting the conclusions of Ref. [13] has been demonstrated simultaneously in Ref. [27], where its consequences for identifying Dirac-magnon materials are discussed.

*Corresponding author.
Stanislav.Nikitin@psi.ch

[1] K. S. Novoselov, A. K. Geim, S. V. Morozov, D. Jiang, Y. Zhang, S. V. Dubonos, I. V. Grigorieva, and A. A. Firsov, Electric field effect in atomically thin carbon films, Science **306**, 666 (2004).
[2] K. S. Novoselov, A. K. Geim, S. V. Morozov, D. Jiang, M. I. Katsnelson, I. V. Grigorieva, S. V. Dubonos, and A. A. Firsov, Two-dimensional gas of massless Dirac fermions in graphene, Nature (London) **438**, 197 (2005).
[3] A. K. Geim, Graphene: Status and prospects, Science **324**, 1530 (2009).
[4] S. S. Pershoguba, S. Banerjee, J. C. Lashley, J. Park, H. Ågren, G. Aeppli, and A. V. Balatsky, Dirac Magnons in Honeycomb Ferromagnets, Phys. Rev. X **8**, 011010 (2018).
[5] F.-Y. Li, Y.-D. Li, Y. B. Kim, L. Balents, U. Yu, and G. Chen, Weyl magnons in breathing pyrochlore antiferromagnets, Nat. Commun. **7**, 12691 (2016).
[6] K. Li, C. Li, J. Hu, Y. Li, and C. Fang, Dirac and Nodal Line Magnons in Three-Dimensional Antiferromagnets, Phys. Rev. Lett. **119**, 247202 (2017).
[7] P. McClarty, Topological magnons: A review, Annu. Rev. Condens. Matter Phys. **13**, 171 (2022).
[8] A. Mook, K. Plekhanov, J. Klinovaja, and D. Loss, Interaction-Stabilized Topological Magnon Insulator in Ferromagnets, Phys. Rev. X **11**, 021061 (2021).
[9] W. Yao, C. Li, L. Wang, S. Xue, Y. Dan, K. Iida, K. Kamazawa, K. Li, C. Fang, and Y. Li, Topological spin excitations in a three-dimensional antiferromagnet, Nat. Phys. **14**, 1011 (2018).
[10] L. Chen, J.-H. Chung, B. Gao, T. Chen, M. B. Stone, A. I. Kolesnikov, Q. Huang, and P. Dai, Topological Spin Excitations in Honeycomb Ferromagnet CrI_3, Phys. Rev. X **8**, 041028 (2018).

[11] B. Yuan, I. Khait, G.-J. Shu, F. C. Chou, M. B. Stone, J. P. Clancy, A. Paramekanti, and Y.-J. Kim, Dirac Magnons in a Honeycomb Lattice Quantum *XY* Magnet $CoTiO_3$, Phys. Rev. X **10**, 011062 (2020).

[12] M. Elliot, P. A. McClarty, D. Prabhakaran, R. D. Johnson, H. C. Walker, P. Manuel, and R. Coldea, Order-by-disorder from bond-dependent exchange and intensity signature of nodal quasiparticles in a honeycomb cobaltate, Nat. Commun. **12**, 3936 (2021).

[13] Z. Cai, S. Bao, Z.-L. Gu, Y.-P. Gao, Z. Ma, Y. Shangguan, W. Si, Z.-Y. Dong, W. Wang, Y. Wu, D. Lin, J. Wang, K. Ran, S. Li, D. Adroja, X. Xi, S.-L. Yu, J.-X. Li, and J. Wen, Topological magnon insulator spin excitations in the two-dimensional ferromagnet $CrBr_3$, Phys. Rev. B **104**, L020402 (2021).

[14] A. Scheie, P. Laurell, P. A. McClarty, G. E. Granroth, M. B. Stone, R. Moessner, and S. E. Nagler, Dirac Magnons, Nodal Lines, and Nodal Plane in Elemental Gadolinium, Phys. Rev. Lett. **128**, 097201 (2022).

[15] A. V. Chumak, V. I. Vasyuchka, A. A. Serga, and B. Hillebrands, Magnon spintronics, Nat. Phys. **11**, 453 (2015).

[16] X. S. Wang, H. W. Zhang, and X. R. Wang, Topological Magnonics: A Paradigm for Spin-Wave Manipulation and Device Design, Phys. Rev. Applied **9**, 024029 (2018).

[17] P. Pirro, V. I. Vasyuchka, A. A. Serga, and B. Hillebrands, Advances in coherent magnonics, Nat. Rev. Mater. **6**, 1114 (2021).

[18] L. Chen, M. B. Stone, A. I. Kolesnikov, B. Winn, W. Shon, P. Dai, and J.-H. Chung, Massless Dirac magnons in the two dimensional van der Waals honeycomb magnet $CrCl_3$, 2D Mater. **9**, 015006 (2022).

[19] See Supplemental Material at http://link.aps.org/supplemental/10.1103/PhysRevLett.129.127201 which contains Refs. [20–22], for a full exposition of our data reduction and fitting, of the bin-width error that can appear as a gap at the Dirac point, of the intensity winding property at this point, of the comparison with literature results, and of the adapted SWT calculations we perform to obtain the first-order magnon self-energy in the J_1-J_2-J_3 model.

[20] E. Xiao, H. Ma, M. S. Bryan, L. Fu, J. M. Mann, B. Winn, D. L. Abernathy, R. P. Hermann, A. Khanolkar, C. A. Dennett, D. H. Hurley, M. E. Manley, and C. A. Marianetti, Validating first-principles phonon lifetimes via inelastic neutron scattering, arXiv:2202.11041.

[21] F. J. Dyson, General theory of spin-wave interactions, Phys. Rev. **102**, 1217 (1956).

[22] F. J. Dyson, Thermodynamic behavior of an ideal ferromagnet, Phys. Rev. **102**, 1230 (1956).

[23] B. Morosin and A. Narath, X-ray diffraction and nuclear quadrupole resonance studies of chromium trichloride, J. Chem. Phys. **40**, 1958 (1964).

[24] E. J. Samuelsen, R. Silberglitt, G. Shirane, and J. P. Remeika, Spin waves in ferromagnetic $CrBr_3$ studied by inelastic neutron scattering, Phys. Rev. B **3**, 157 (1971).

[25] M. A. McGuire, H. Dixit, V. R. Cooper, and B. A. Sales, Coupling of crystal structure and magnetism in the layered, ferromagnetic insulator CrI_3, Chem. Mater. **27**, 612 (2015).

[26] H. Wang, V. Eyert, and U. Schwingenschlögl, Electronic structure and magnetic ordering of the semiconducting chromium trihalides $CrCl_3$, $CrBr_3$, and CrI_3, J. Phys. Condens. Matter **23**, 116003 (2011).

[27] S.-H. Do, J. A. M. Paddison, G. Sala, T. J. Williams, K. Kaneko, K. Kuwahara, A. F. May, J. Yan, M. A. McGuire, M. B. Stone, M. D. Lumsden, and A. D. Christianson, Gaps in topological magnon spectra: Intrinsic vs extrinsic effects, Phys. Rev. B **106**, L060408 (2022).

[28] W. B. Yelon and R. Silberglitt, Renormalization of large-wave-vector magnons in ferromagnetic $CrBr_3$ studied by inelastic neutron scattering: Spin-wave correlation effects, Phys. Rev. B **4**, 2280 (1971).

[29] https://www.ill.eu/users/instruments/instrument-list/panther.

[30] S. E. Nikitin, B. Fåk, K. W. Krämer, and C. Rüegg, Temperature-induced evolution of topological magnons in $CrBr_3$ (Institut Laue-Langevin (ILL) Grenoble, 2021), 10.5291/ILL-DATA.DIR-236.

[31] U. Stuhr, B. Roessli, S. Gvasaliya, H. M. Rønnow, U. Filges, D. Graf, A. Bollhalder, D. Hohl, R. Bürge, M. Schild, L. Holitzner, C. Kaegi, P. Keller, and T. Mühlebach, The thermal triple-axis-spectrometer EIGER at the continuous spallation source SINQ, Nucl. Instrum. Methods Phys. Res., Sect. A **853**, 16 (2017).

[32] O. Arnold *et al.*, Mantid—Data analysis and visualization package for neutron scattering and μSR experiments, Nucl. Instrum. Methods Phys. Res., Sect. A **764**, 156 (2014).

[33] R. A. Ewings, A. Buts, M. D. Le, J. van Duijn, I. Bustinduy, and T. G. Perring, HORACE: Software for the analysis of data from single crystal spectroscopy experiments at time-of-flight neutron instruments, Nucl. Instrum. Methods Phys. Res., Sect. A **834**, 132 (2016).

[34] S. Toth and B. Lake, Linear spin wave theory for single-Q incommensurate magnetic structures, J. Phys. Condens. Matter **27**, 166002 (2015).

[35] V. A. Alyoshin, V. A. Berezin, and V. A. Tulin, rf susceptibility of single-crystal $CrBr_3$ near the Curie temperature, Phys. Rev. B **56**, 719 (1997).

[36] S. Shivam, R. Coldea, R. Moessner, and P. McClarty, Neutron scattering signatures of magnon Weyl points, arXiv:1712.08535.

[37] J. F. Dillon, Ferromagnetic resonance in $CrBr_3$, in *Proceedings of the Seventh Conference on Magnetism and Magnetic Materials* (Springer, New York, 1962), p. 1191.

[38] F. Bloch, Zur Theorie des Ferromagnetismus, Z. Phys. **61**, 206 (1930).

[39] J. Becker and S. Wessel, Diagnosing Fractionalization from the Spin Dynamics of Z_2 Spin Liquids on the Kagome Lattice by Quantum Monte Carlo Simulations, Phys. Rev. Lett. **121**, 077202 (2018).

[40] H. Shao and A. W. Sandvik, Progress on stochastic analytic continuation of quantum Monte Carlo data, arXiv:2202.09870.

[41] V. Zauner-Stauber, L. Vanderstraeten, J. Haegeman, I. P. McCulloch, and F. Verstraete, Topological nature of spinons and holons: Elementary excitations from matrix product states with conserved symmetries, Phys. Rev. B **97**, 235155 (2018).

[42] B. Ponsioen, F. F. Assaad, and P. Corboz, Automatic differentiation applied to excitations with projected entangled pair states, SciPost Phys. **12**, 006 (2022).